18th International Conference on Space Operations, Montreal, Canada, 26 - 30 May 2025.

SpaceOps-2025, ID # 308

Hybrid Autonomous Global Localization in the Absence of PNT Infrastructure

Charles H. Lee[a]*, Kar-Ming Cheung[b], William W. Jun[c]

[a] *Jet Propulsion Laboratory, California Institute of Technology, California, USA, Charles.h.lee@jpl.nasa.gov*
[b] *Jet Propulsion Laboratory, California Institute of Technology, California, USA, Kar-ming.cheung@jpl.nasa.gov*
[c] *Jet Propulsion Laboratory, California Institute of Technology, California, USA, William.w.jun@jpl.nasa.gov*
* Corresponding Author

Abstract

Typical global positioning methods require a network of multiple satellites for localization. When such a GPS-like infrastructure is unavailable or when its direct line-of-sight communications with Earth are not warranted, a user on the far side of the moon or near the polar regions would need to rely on other autonomous navigation techniques such as celestial positions, local radiometric infrastructure network, altimetry, and terrain-relative measurements, etc. to determine its in-situ position and orientation.

This paper proposes a hybrid scheme combining Inertial Measurement Unit (IMU) sensors, star trackers (ST), and surrounding terrain outline (STO) for real-time autonomous localization. The lack of oceans and plateaus and the excess of craters and ridges on the moon help make an STO a signature unique to its location. Due to the absence of vegetation, seasons, weather, and artificial human-made structures on the moon, STOs remain unchanged over time. In addition, since all rovers are equipped with onboard panoramic cameras, STOs can be obtained readily and reasonably inexpensive. Some cameras have infrared capabilities, enabling the rover to self-localize in complete darkness or low-lighting conditions. Due to the contrast between the cold sky background, the moon's diffusing hot body temperature, and the unavailability of the atmosphere, an STO can be obtained very crisply and distinguishably. Once collected, the STO can be matched with a database of constructed STOs for a specific region to determine the position and orientation of the user. The STO database is built in advance using NASA's high-resolution digital elevation map (DEM), acquired by the Lunar Orbiter Laser Altimeter (LOLA) instrument on the Lunar Reconnaissance Orbiter (LRO).

Our previous investigations show that, with appropriate instrument calibration and performance, the average self-localization errors can be a few meters to tens of meters, and the average orientation errors are within half a degree. For high accuracy results, the terrain outline matching method requires high-resolution DEM, and thus intensive computational effort and large memory storage. On the other hand, recent advanced star trackers can provide the user's attitude and position within a few seconds, even in lost-in-space mode. However, their three-sigma position errors could be as high as tens of meters. Our proposed scheme first employs the ST technique to attain a quick approximate position and then applies the STO method on a high-resolution DEM but small area enclosing the approximate position. This way, we can achieve accuracy and speed by combining the ST and the STO techniques. Our results show that even at the worst tilting and terrain uncertainties and half of the field of view being blocked, the 3σ positioning error for the STO is less than 5m. When 75% of the field of view is obstructed, the 3σ positioning errors never exceed 25m. Most importantly, the STO method works in areas with relatively flat local terrain.

Keywords: Autonomous surface localization, surrounding terrain outline, horizon matching technique, positioning without PNT satellites, star-trackers, IMU sensors.

1. Introduction

Traditional global positioning methods require a network of multiple satellites for localization. When such a GPS-like infrastructure is unavailable or when its direct line-of-sight communications with Earth are not guaranteed, a user on the far side of the moon or near the polar regions will count on other autonomous navigation techniques, such as celestial positions, local radiometric infrastructure network, altimetry, and terrain-relative measurements, to determine its position and orientation. In the early phases of the cislunar PNT network, the number of service satellites may be limited, and precise localization with a few satellites is possible. However, the process would depend on the in-view satellite coverage and require a long tracking time, rendering it implausible for real-time navigation.

On the other hand, existing vision-based algorithms would require users to match collected images of known landmarks with high-resolution overhead orbital orthoimages. During the Apollo era, the user's localization and orientation could be determined by aligning panorama photos taken by the Apollo Lunar Surface Experiments Package (ALSEP) instrument with orbital orthoimages. This approach requires distinctive markers visible on the panorama and orbital images. A subsequent study [1] in 2012, using the Lunar Reconnaissance Orbiter's (LRO) narrow-angle camera and a least-squares fit, yields the positions of the camera and the ALSEP equipment with an accuracy of one pixel (0.25m). With the advances in mountain detection in images, several algorithms for automatic self-position estimation were developed in [2]. The approach is to search for mountain peaks in a panorama image and a given orthographic map and maximize the position's posterior probability given the directions to the mountains [3]. These algorithms were tested with Earth and Apollo-17 images, and the accuracies were approximately 91 meters.

More innovative algorithms were developed during the early Mars rover missions. An automated range map matching algorithm was tested on the Mars Sojourner to estimate its position [4]. The approach maximizes the likelihood of matching local panorama images and the orbital map of surrounding landmark structures. The average errors were in the tenths of meters. A similar approach, coupled with visual odometry and Mars Global Surveyor's narrow-angle camera images, was used to estimate the landing positions of the Mars Exploration Rovers, Spirit [5] and Opportunity [6]. A fully automatic global localization algorithm that minimizes the least square distance between the rover's 3D stereo image and the orbital terrain map was proposed in [7]. The approach was tested on the Mars Science Laboratory's data and yielded the rover's position 87% of the time with a 10m accuracy. These methods require a great deal of ground-in-the-loop efforts and are impractical for in-situ operations. Other methods use crater shadows or beacons from known markers. These methods require correct lighting conditions, operating in well-cognizant areas, or involving humans in the loop.

More recently, Matthies et al. in [8] and Cauligi et al. in [9] proposed an onboard localization method using craters as landmarks, where craters were detected using laser lidar, stereo vision, and monocular images. Although their approach is a localization scheme that can operate similarly in complete darkness and yields an absolute localization error of less than 10 meters, it relies on more complicated machinery and computation to determine the rover's position. This approach is at least one more dimensional than ours. Namely, their approach uses AI to detect the edges of the landmarks (craters), then registers the acquired 3D image and compares it with the emulated images constructed from past overflights. Our proposed method deals with 1D curves, whereas the technique in [9] works with 3D surfaces, which may not be practical for a small rover to operate autonomously in real-time.

2. Autonomous Localization Using Surrounding Terrain Outline

2.1 Surrounding Terrain Outline

In this subsection, we describe the terrain outline surrounding a user for real-time autonomous localization. A surrounding terrain outline (STO) is where the sky meets the land; an example is shown in Figure 1. The moon's fullness of craters and ridges and lack of oceans and plateaus help make an STO a signature unique to its location. In addition, each STO remains unchanged over time due to the absence of vegetation, seasons, weather, and artificial human-made structures on the moon.

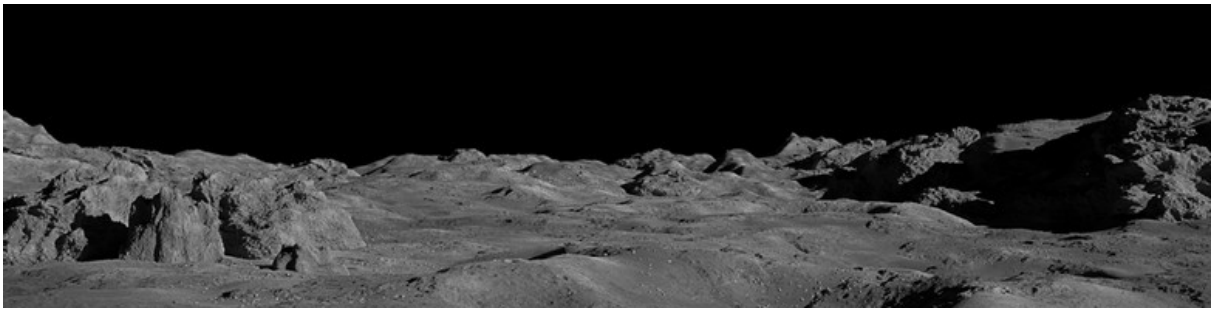

Figure 1. Example of Surrounding Terrain Outline on the Moon

Obtaining an STO is relatively inexpensive. An STO can be readily and easily captured using onboard panoramic cameras. Figure 2a displays a Mars rover equipped with a suite of cameras, ranging from MastCams to PanCams,

SuperCams, HazCams, etc. Some cameras come with infrared capabilities, which enable the rover to attain the STO even in complete darkness. Due to the contrast between the cold sky background, the moon's diffusing hot body temperature, and the lack of atmosphere, an STO can be obtained very crisply and distinguishably. Figure 2b shows images collected using infrared sensors under different wavelengths.

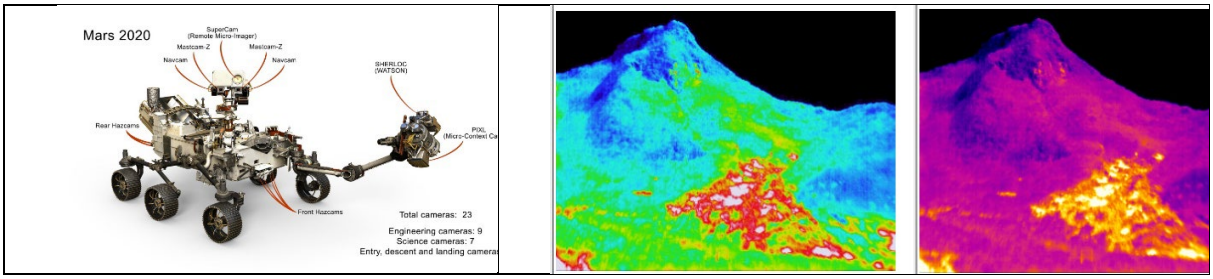

Figures 2a. Mars Curiosity Rover with its onboard cameras (left) and 2b. Infrared images attained under different wavelengths (center and right)

2.2 Constructing STO Database

Once collected, the user's STO can be matched with a database of constructed STOs for a specific region to determine the position and orientation of the user. An STO database can be built in advance using a digital elevation model (DEM) map. NASA has maintained a database of DEM maps at different resolutions for the Moon and Mars. Terrain elevation values were acquired by the Lunar Reconnaissance Orbiter (LRO) and Mars Global Surveyor (MGS) by the Lunar Orbiter Laser Altimeter (LOLA) and the Mars Orbiter Laser Altimeter (MOLA) instruments, respectively. Our analysis focuses on the 5m-resolution DEM data, approximately 100km around the lunar south pole. The elevations for the region are shown in Figure 3a, and they range from ~ -4000m to ~2000m. The maximum latitude is 87° South. The corresponding slopes are displayed in Figure 3b. Here, the slopes are steeper inside craters, especially the Shackleton crater in the center.

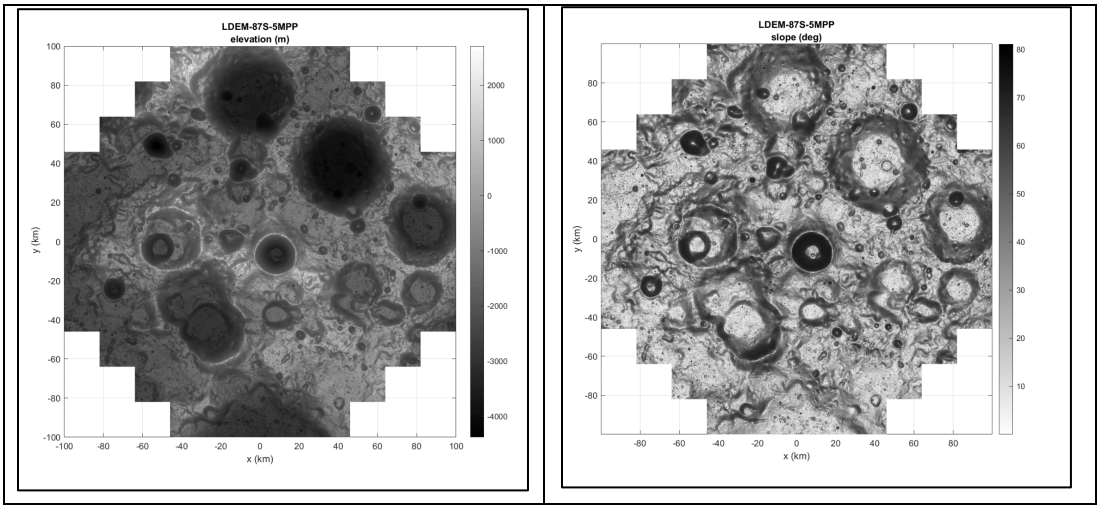

Figures 3a. 5m-resolution NASA LOLA DEM elevations at the lunar south pole (left) and 3b. The corresponding slopes (right)

We next discuss how the STOs are computed a priori from the terrain DEM data. A three-dimensional surface for the Lunar South Pole region is constructed by combining the LOLA terrain DEM with the lunar spheroid. Thus, the position vector of a user at any known longitude and latitude can be found. The height of the camera/sensor instrument on the rover is assumed to be h meters above the surface, and its unit normal vector (zenith) is assumed to originate from the center of the moon to the user's position. The elevation mask in each azimuth must be computed to emulate the user's STO from a known location and height. When gazing in an azimuthal direction, the user must search for a horizon mask angle φ, where the separation of the sky and the terrain occurs (the left of Figure 4). Given any object in the sky, the elevation angle of the object must exceed this horizon mask angle φ to be in view with it. To determine

the value of φ, we consider all the available discrete points in the DEM data set in that direction. The graph on the right of Figure 4 displays four such points for demonstration. They are color-coded; each produces a horizon angle, and the largest yields the horizon mask in that direction. The process is repeated for every azimuth at one-degree resolution. Examples of STOs from four random locations are displayed in Figure 5. With sufficient height and clearance, a user can see below the horizon. In that case, the horizon mask is negative. The mask construction is very computationally intensive but can be calculated in advance. It takes approximately less than a second on a personal laptop to compute the STO from a location.

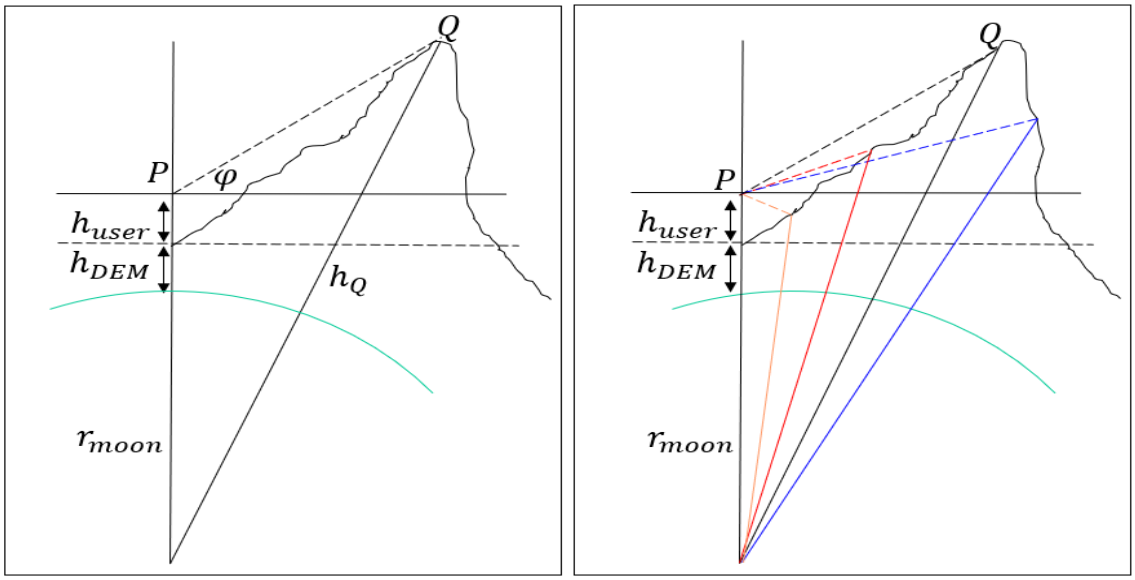

Figure 4. The terrain outline for each azimuth is determined by finding the maximum elevation of all possible points in the DEM data set in that direction.

In our paper, we assume the STOs for the lunar south pole region have been computed a priori using the algorithm described above. For our self-localization algorithm, we assume the lunar asset is inside an area with no knowledge of its previous location or orientation. This scenario is similar to a rover that has just landed or is taking an excursion in a nearby vicinity.

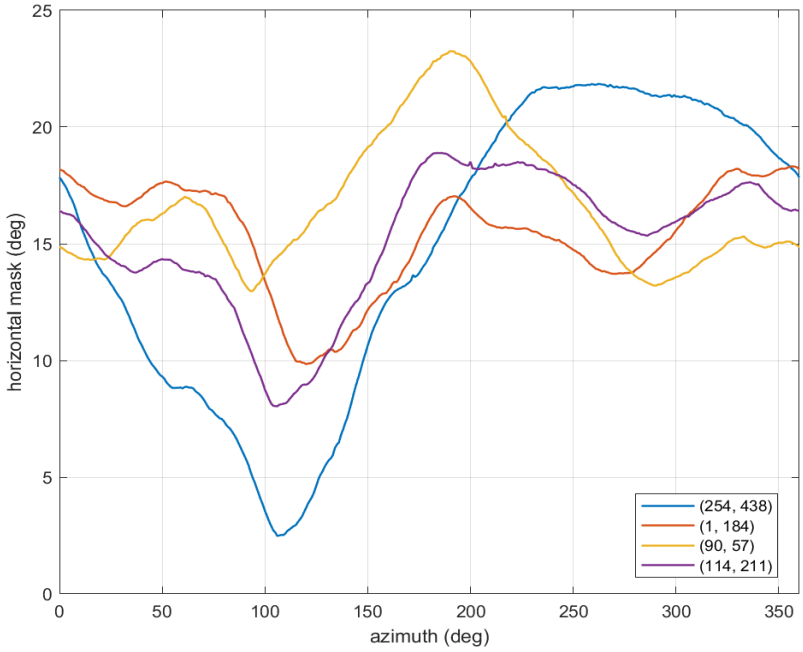

Figure 5. Examples of surrounding terrain outline from four random locations.

2.3 Localization and Orientation Determination using STO Observations

We denote by $\boldsymbol{m}_{x_o,y_o}(az)$ the local STO mask collected by a user at the location (x_o, y_o) and in the azimuth direction az. Note that (x_o, y_o) is in the polar stereographic coordinate, and it corresponds to an (i^*, j^*) pixel in the LOLA's terrain DEM data. Let θ be the user's orientation angle, then its observed mask is $\boldsymbol{m}_{x_o,y_o}(az + \theta)$, which is a mere rotation of the STO by the angle θ. Our proposed algorithm determines the user's location and orientation by scanning through the previously computed STOs $\boldsymbol{m}_{x,y}(az)$ and all possible orientations, seeking the one with the largest resemblance. The resemblance of the observed and the database STOs can be computed using their correlation,

$$f(x, y, \theta) = \langle \boldsymbol{m}_{x_o,y_o}(az + \theta), \boldsymbol{m}_{x,y}(az) \rangle,$$
$$\text{where } 0 \le \theta \le 360°, 0 \le az \le 360°, \quad (1)$$
$$x_{min} \le x \le x_{max} \text{ and } y_{min} \le y \le y_{max}.$$

The values of $x_{min}, x_{max}, y_{min}$, and y_{max} are the bounds of an area where the user is located. We assume that the STO profiles are normalized with respect to the azimuth. Thus, the correlation function in (1) carries values between -1 and 1, with 1 being a perfect match.

A discretized version of the correlation of two STOs can be expressed as,

$$f(i, j, \theta) = \langle \boldsymbol{m}_{i^*,j^*}(az + \theta), \boldsymbol{m}_{i,j}(az) \rangle,$$
$$\text{where } 0 \le \theta \le 360°, 0 \le az \le 360°, \quad (2)$$
$$1 \le i \le N_x \text{ and } 1 \le j \le N_y.$$

We consider a 4km by 5km area at the Connecting Ridge next to the Shackleton Crater for our simulations. The region has 800x1000 or 800,000 pixels, and the storage for the 360-deg STOs in MATLAB binary format is approximately 2 GB. As seen in Figure 5, each pixel bears a distinctive STO that resembles a signature.

The main objective of this paper is to demonstrate the feasibility of the approach. In another paper, the efficiency and robustness of the algorithm and optimization techniques using Machine Learning and Artificial Intelligence are discussed [12]. For now, we search for the maximum correlation using the exhaustive search. Specifically, we calculate the correlation in (2) for all possible values of θ, i, and j, The largest yields the user's location and orientation. Due to our problem setup, the best accuracies would be within one pixel for the position and one degree for the orientation.

The surface user's STOs must be emulated to test our localization algorithms. We start with a known horizon mask at the (i^*, j^*) pixel. We assume that the rover is equipped with an inclinometer so that the normal vector from the moon's center to the user's location is known. Thus, the first source of error is the bias of the normal vector being tilted away from the true normal in a random direction α by a random angle β. The tilting error can be characterized by the function,

$$\boldsymbol{T}(\alpha, \beta) = \beta \cos(az - \alpha). \quad (3)$$

The random direction α is assumed to have a uniform distribution with values between 0° and 360°. The random tilt angle β is assumed to be normally distributed with the variance σ_{tilt}. The second source is the mask reading error at each azimuth $\boldsymbol{e}_{read}$. Such reading errors could come from the user's instrument or mask calculation using the LOLA DEM data. The random mask error in each azimuthal direction is also assumed to be normally distributed with variance σ_{read}. We also consider additional cases where the instrument cannot register due to reading ambiguity, planetary/solar glare, or vehicle obstruction. In our study, there are cases when we assume 0% to 75% of the azimuths are missing.

$$\boldsymbol{m}_u(\theta) = \boldsymbol{T}(\alpha, \beta)\, \boldsymbol{m}_{i^*,j^*}(az + \theta) + \boldsymbol{e}_{read}. \quad (4)$$

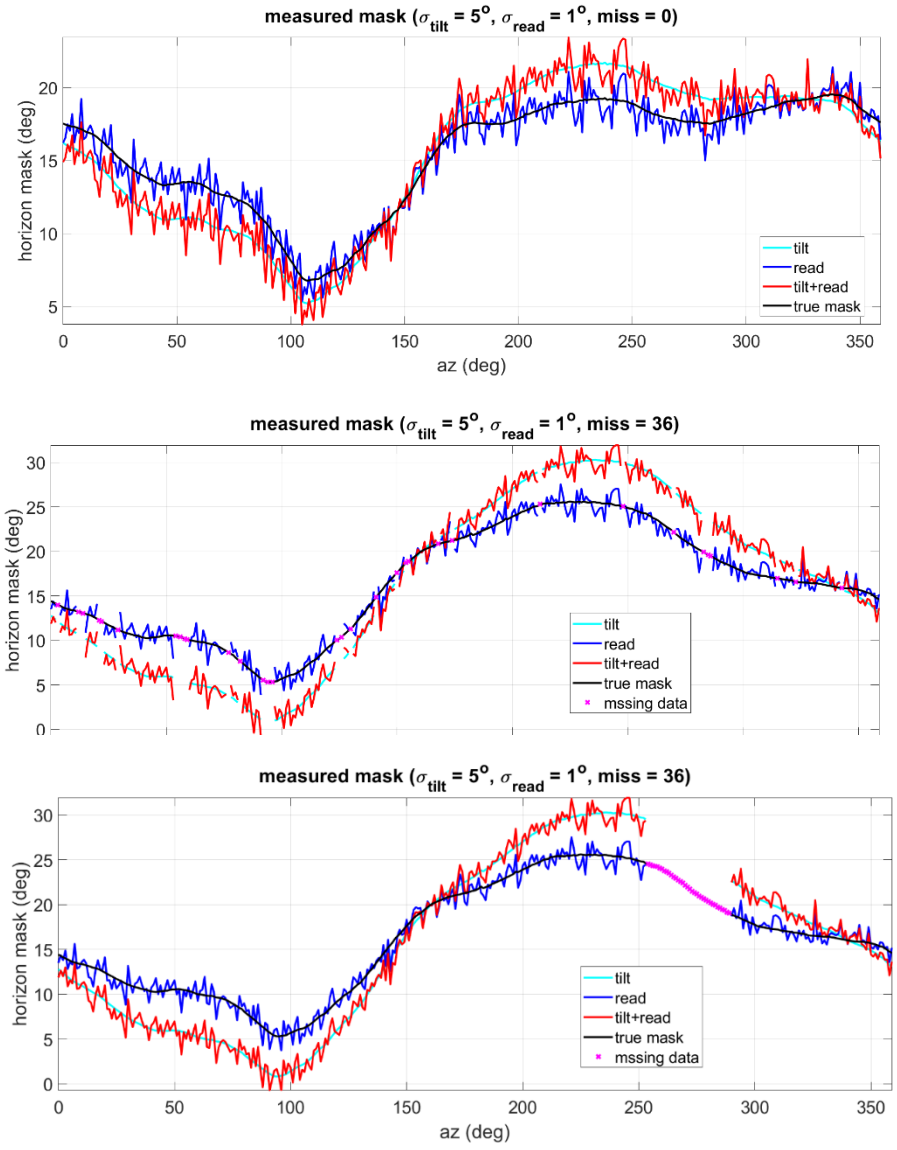

Figure 6. Examples of STOs with $\sigma_{read} = 1°$ and $\sigma_{tilt} = 5°$; no missing data (top), 10% noncontiguous data missing (middle), and 10% contiguous data missing (bottom).

Examples of simulated user's STOs are displayed in Figure 6 at a random location with $\sigma_{read} = 1°$ and $\sigma_{tilt} = 5°$. Each graph contains four user's horizon masks:

(i) user's true STO (black),
(ii) STO with random tilt (cyan),
(iii) STO with random reading errors (blue) and
(iv) STO with random tilt and reading errors (red).

The top figure shows the STO with no missing data, and the middle and bottom graphs show the STOs with random non-contiguous and random contiguous missing data, respectively. Azimuths for which the mask data are missing are marked with magenta x's. In extreme cases, the shape of the masks could be severely deformed, leading to wrong geo-localization conclusions.

Preliminary work has been tested using NASA's LOLA 20m DEM data, where the user's STO was assumed to be the constructed STO but distorted by random tilting biases and instrument errors. Our brute-force correlation maximization results show the approach is promising [10], with positioning errors ranging from a few meters to 10 meters and orientation errors of less than half a degree.

2.4 Hybrid Localization Scheme

A direct exhaustive search for the position and orientation of a user could be time-consuming, especially when the search terrain area is large, and the resolution is high. The most effective way to speed up the STO algorithm is to limit its search space, which can be accomplished by employing additional equipped sensors to narrow the potential solution space to a smaller region.

In our case, we attempt to use a commercial-off-the-shelf (COTS) star tracker named Hydra. Its descriptions and specifications can be found in [11]. Actual images of the stars at the user's location are not available. The first part of this study is to emulate the stars in the sky observed by the user. A list of stars with a visual magnitude of 6 or less, excluding the planets, can be extracted from the star catalog. There are approximately over 5 thousand of such stars. With a known temporal epoch, the appearances of the stars in the lunar planetocentric coordinate are known. Suppose the user's actual location and attitude are assumed to be $\boldsymbol{x}^{true} = \langle x_{lon}^{true},\ x_{lat}^{true}, x_{alt}^{true} \rangle$ and $\boldsymbol{y}^{true} = \langle y_{yaw}^{true},\ y_{pitch}^{true}, y_{roll}^{true} \rangle$, respectively. So that the star's true azimuth and elevation angles $\boldsymbol{s}^{true} = \langle \boldsymbol{s}_{az}^{true},\ \boldsymbol{s}_{elev}^{true} \rangle$ with respect to the local topocentric coordinates are available. For each realization, we attain reading from no more than 64 brightest stars within a random field of view of 21°. Random noises are also added to the observation reading

$$\boldsymbol{s}_{az}^{obs} = \boldsymbol{s}_{az}^{true} + \boldsymbol{n_{az}} \text{ and } \boldsymbol{s}_{az}^{obs} = \boldsymbol{s}_{elev}^{true} + \boldsymbol{n_{elev}}. \quad (4)$$

Hydra's 3σ values of the azimuth and the elevation range from 0.6 to 3.4 arcsec and 4.6 to 27 arcsec, respectively, depending on the high or low frequency spatial error.

Note that the star tracker can identify the stars based on their brightness, formation, and pattern from the observation. Once the stars in the observation have been recognized, we proceed to determine the user's location $\boldsymbol{x} = \langle x_{lon},\ x_{lat},\ x_{alt} \rangle$ and attitude $\boldsymbol{y} = \langle y_{yaw},\ y_{pitch},\ x_{roll} \rangle$.

The process of finding the user's position and attitude can be done iteratively, starting with some initial guess $\boldsymbol{x}^{(0)} = \langle x_{lon}^{(0)},\ x_{lat}^{(0)},\ x_{alt}^{(0)} \rangle$ and $\boldsymbol{y}^{(0)} = \langle y_{yaw}^{(0)},\ y_{pitch}^{(0)}, y_{roll}^{(0)} \rangle$. The subsequent solution is determined via an optimization process, and the following steps and cost function assesses its performance:

(1) Based on the current approximate position $\langle x_{lon}^{(n)},\ x_{lat}^{(n)},\ x_{alt}^{(n)} \rangle$ and time, a topological coordinate system $\langle \boldsymbol{V}_{east}^{(n)},\ \boldsymbol{V}_{north}^{(n)},\ \boldsymbol{V}_{up}^{(n)} \rangle$ can be found.

(2) Based on the current approximate attitude $\langle y_{yaw}^{(n)},\ y_{pitch}^{(n)}, y_{roll}^{(n)}\rangle$ and the list of recognized stars, their approximate azimuths and elevations $\langle \boldsymbol{s}_{az}^{(n)},\ \boldsymbol{s}_{elev}^{(n)}\rangle$ can be found.

(3) The performance of the current approximate position and attitude can be assessed by the cost function

$$C\left(\boldsymbol{x}^{(n)},\ \boldsymbol{y}^{(n)}\right) = \left\| \langle \boldsymbol{s}_{az}^{(n)},\ \boldsymbol{s}_{elev}^{(n)}\rangle - \langle \boldsymbol{s}_{az}^{(obs)},\ \boldsymbol{s}_{elev}^{(obs)}\rangle \right\|. \qquad (5)$$

(4) Other constraints, such as the user's attitude, can also be added.

The minimizer, when converges, yields the best set of position and attitude $(\boldsymbol{x}^*,\ \boldsymbol{y}^*)$ that matches the azimuths and elevations of the recognized stars of the observables.

3. Case Studies

There are two parts to our case studies. The first focuses on using star trackers to reduce the search space for the STO technique, and the second part shows the localization results using the STO method with high-resolution DEM data.

3.1 Reducing STO's Search Space Using Star Tracker and IMU Sensors

We assess the search space reduction technique before the STO using Lunar Endurance's 12 sampling sites. NASA's Lunar Endurance is a proposed rover mission that transverses autonomously over 1000 km on the lunar far side to collect samples and deliver them to Starship for returning to Earth. In our numerical studies, we assume our star tracker is Hydra with the specifications of the 21-deg field of view and no more than 64 stars with visual magnitude ≤ 6. Noises are added to the observed stars' azimuths and elevations. Depending on the frequency spatial error, Hydra's 3σ-values for the azimuths and elevation range from 0.6 to 3.4 arcsec and 4.6 to 27 arcsec, respectively. Three scenarios are considered:

(1) Determine user's position $\boldsymbol{x}$ assuming attitude knowledge by other means, such as the IMU.
(2) Determine user's position $\boldsymbol{x}$ assuming attitude and altitude knowledge by other means, such as the IMU.
(3) Determine user's position $\boldsymbol{x}$ and attitude $\boldsymbol{y}$ assuming attitude and altitude approximation by other means, such as the IMU.

In the first two scenarios, we only search for the user's position $\boldsymbol{x} = \langle x_{lon},\ x_{lat},\ x_{alt}\rangle$. The attitude is assumed to be approximated from previous step or other means such as the IMU. The minimization process yields the optimal solution with the cost function specified in Equation (5). In the second scenario, we also assume that the user's altitude knowledge has some errors (3σ-altitude=10m). Results for the first two scenarios are summarized in Table 1. The 3σ-position values for East/West, North/South, Up/Down, and 3D are recorded. Twelve sampling sites were used, and the results seem site-independent. The altitude with some uncertainties can be approximated, and the accuracy can be improved. In our case, the 3D-positioning errors went from 60's to 40's meters.

Table 1: 3σ positioning errors at different sites with and without altitude constraint.

Endurance Site Number	Longitude (deg)	Lattitude (deg)	3σ Positioning Error (m) w/o Altitude Constraint				3σ Positioning Error (m) with Altitude Constraint			
			East/West	North/South	Up/Down	3D	East/West	North/South	Up/Down	3D
1	-161.8022	-57.8621	43.710	32.465	54.805	64.483	39.705	32.242	23.126	45.730
2	-162.4138	-57.3560	44.813	27.187	56.943	66.376	39.738	27.959	25.142	46.423
3	-166.6533	-56.6008	41.962	23.392	54.895	63.312	34.042	23.486	22.876	40.878
4	-170.8276	-55.4248	46.835	22.789	57.480	64.348	32.237	23.147	22.709	39.982
5	-171.9308	-57.2341	43.041	25.762	57.089	65.813	33.346	25.431	21.692	38.859
6	176.5608	-61.2595	43.838	19.360	57.652	64.423	34.226	18.994	19.602	39.836
7	162.6293	-57.2223	44.929	25.943	55.476	64.593	31.579	23.391	21.999	39.008
8	161.0510	-59.1245	41.852	24.749	57.580	64.293	33.101	21.662	21.123	40.354
9	162.4302	-64.9294	40.251	23.807	56.460	64.359	36.142	24.925	17.697	42.242
10	135.3675	-73.4034	29.469	27.240	60.927	64.753	27.946	27.761	12.275	40.074
11	139.3307	-75.2993	30.159	23.688	60.429	64.211	30.442	25.256	11.103	39.908
12	-137.2392	-89.4390	27.125	24.767	57.708	64.305	27.148	24.788	5.613	36.764

The third scenario resembles the lost in space case, where we do not assume we have any knowledge of the attitude, and we optimize for both the user's position $\boldsymbol{x} = \langle x_{lon},\ x_{lat},\ x_{alt} \rangle$ and attitude $\boldsymbol{y} = \langle y_{yaw},\ y_{pitch},\ x_{roll} \rangle$. We only impose the altitude constraint with a 10m 3σ-uncertainty. Two different sets of Hydra's errors are assumed: the low (3σ-xy = 0.6 arcsec and 3σ-z = 4.6 arcsec) and the high (3σ-xy = 3.4 arcsec and 3σ-z = 27 arcsec) frequency spatial errors. The 3σ-position values for East/West, North/South, Up/Down, and 3D are recorded similarly. The results are displayed in Table 2. Again, the results are site-independent. As expected, the 3D-positioning errors are directly related to the assumed uncertainties. The 3D positioning errors are in the ~40's and 210 meters for the low and high frequency spatial errors, respectively. The 3σ-attitude errors for both cases are no more than 12 arcsec. Although the errors seem slightly higher than in the previous two cases, these results are more realistic and challenging.

Table 2: 3σ positioning and attitude errors at different sites and uncertainties

Endurance Sampling Site Number	3σ-xy = 0.6 arcsec, 3σ-z = 4.6 arcsec, 3σ-Alt = 10m							3σ-xy = 3.4 arcsec, 3σ-z = 27 arcsec, 3σ-Alt = 10m						
	3σ Abs Positioning Error (m)				3σ Abs. Att. Error (arcsec)			3σ Abs Positioning Error (m)				3σ Abs. Att. Error (arcsec)		
	E-W	N-S	U-D	3D	Pitch	Yaw	Roll	E-W	N-S	U-D	3D	Pitch	Yaw	Roll
1	32.323	20.862	30.571	38.940	0.697	1.279	1.943	173.807	120.067	115.300	212.221	4.088	7.498	11.406
2	33.263	21.362	30.114	39.257	0.708	1.350	1.929	174.569	122.244	120.579	217.805	4.156	7.916	11.317
3	32.401	20.234	30.536	40.078	0.696	1.283	2.028	171.366	116.969	114.509	210.630	4.084	7.522	11.901
4	32.398	20.054	30.760	38.991	0.710	1.372	2.045	170.362	116.814	121.648	207.136	4.165	8.042	12.001
5	34.302	18.669	31.176	39.551	0.712	1.374	1.920	174.029	111.276	113.536	212.455	4.179	8.053	11.268
6	32.948	17.086	31.009	40.317	0.661	1.046	1.861	179.934	101.376	101.295	213.795	3.879	6.137	10.915
7	32.694	21.543	31.196	40.154	0.689	1.238	2.017	163.765	127.758	110.271	205.611	4.043	7.259	11.832
8	32.722	21.698	31.177	40.400	0.670	1.115	1.966	167.909	125.519	107.947	211.419	3.933	6.536	11.536
9	32.586	19.805	30.939	39.854	0.614	0.741	1.773	184.614	116.487	92.590	212.230	3.603	4.347	10.401
10	25.587	25.685	29.097	39.345	0.230	0.539	1.383	148.497	146.096	69.589	208.288	1.349	3.164	8.113
11	26.396	23.669	28.646	39.146	0.004	0.504	1.312	155.922	140.419	62.667	214.303	0.020	2.959	7.699
12	25.825	24.022	29.115	37.755	0.228	0.344	0.483	151.238	140.690	28.348	206.633	1.341	2.017	2.836

3.2 Hybrid STO with high-resolution DEM and reduced search space

In this subsection, we focus on the second part of the hybrid scheme for the STO, where a priori technique has been applied and yielded an approximate region for the user. This could result from a short drive from a previously known location or after using the star trackers described in the previous subsection. A 4km by 5km section in the Connecting Ridge near the Shackleton Crater is considered. This area corresponds to an 800x1000 pixels grid of NASA's LOLA DEM at 5m resolution. The elevations and slopes of the region are shown in Figure 7. This region is a good representation due to the variations of elevations and slopes, including many small craters, hillsides, and flat land.

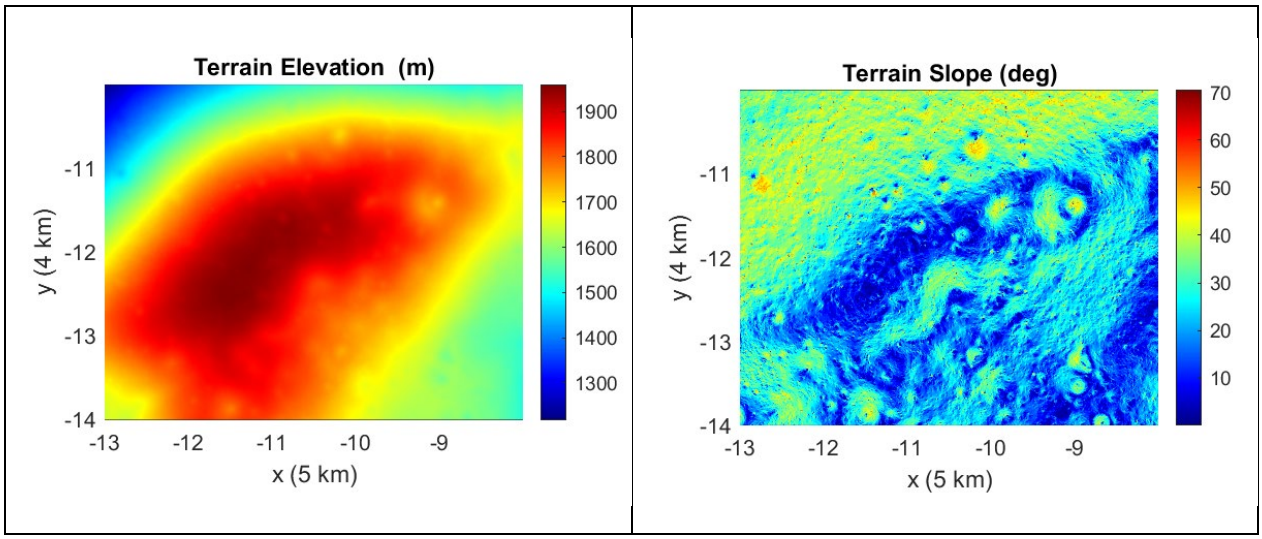

Figure 7: elevations (left) and slopes (right) of 4km by 5km section in the Connecting Ridge near the Shackleton Crater

In our Monte-Carlo study, we randomly pick 10,000 locations in the area, each inside a 150m by 150m or 30x30 pixels box. The Observed STO is assumed to be the user's STO, modified with a random reading/terrain error in every

azimuth direction, a random user's orientation angle, a random tilting direction, and a random tilting angle. The 3σ values for the read/terrain and the tilting angles are assumed to be 60 and 120 arcsec. These are two to four times the specified values of Hydra. We also consider four missing data percentages (0%, 25%, 50%, and 75%) and two missing data types (contiguous and non-contiguous). Examples of the 50% non-contiguous and contiguous missing data are shown in Figure 8. The magenta plus signs in the figure signify where the STO data points are missing.

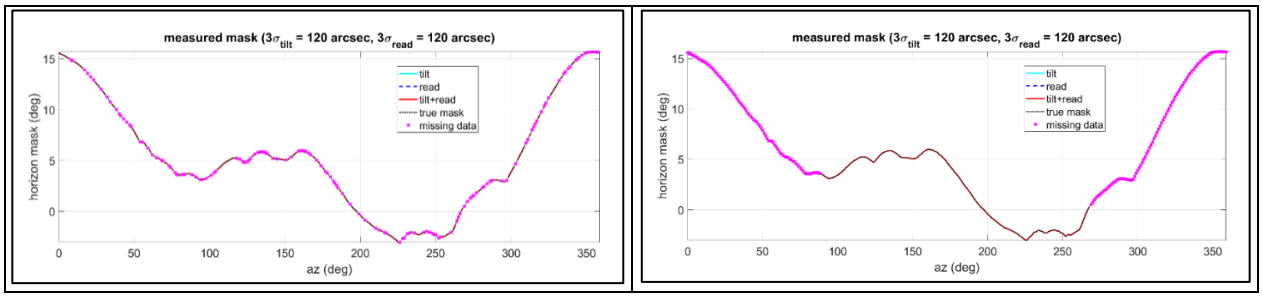

Figure 8: STO with 50% non-contiguous (left) and 50% contiguous (right) missing data

For demonstration purposes, we use the brute-force technique to seek the largest correlation value between the observed STO and the nearby 900 stored STOs. The predicted user's location is the ith - jth pixel that yields the largest correlation. Once the predicted pixel is determined, the positioning error can be calculated using the centers of the predicted and true pixels. The errors are either zero, multiple of the resolution size, or multiple of the resolution size times $\sqrt{2}$. Note that when the error between pixels is zero, the user could be anywhere within the pixel. In this case, the user could be off by at most the pixel size multiplied by $\sqrt{2}/2$, and with our 5m resolution, it could be up to 3.5m. Positioning errors for both the non-contiguous and contiguous missing data are shown in Figure 9. Non-contiguous missing data does not play a significant role. Even though 75% of the STO is missing, its profile and shape persist. The worst-case scenario results are displayed on the right; not only are the tilting and terrain errors high, but three-quarters of the field of view is obstructed. The average position error (~2m) and its 3σ value (~23m) are also shown.

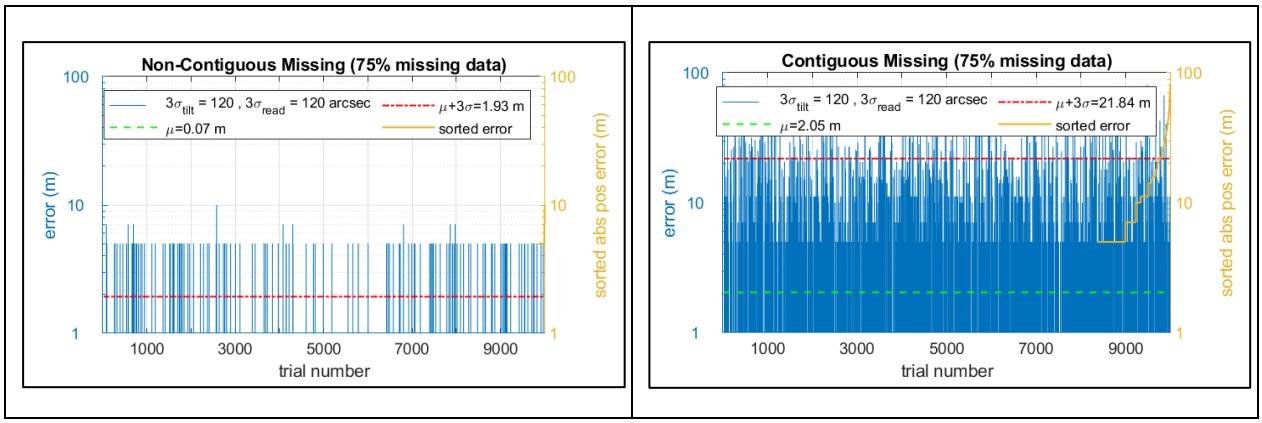

Figure 9: STO errors with 75% non-contiguous (left) and 75% contiguous (right) missing data

The 3σ positioning errors for the STO method are summarized in Table 3. Positioning errors are significant when a large portion of the observed STO is missing, and the missed data is contiguous. Even at the worst tilting and terrain uncertainties and half of the field of view being blocked, the 3σ positioning error is less than 5m. When 75% of the field of view is obstructed, the 3σ positioning error never exceeds 25m.

Table 3: 3σ positioning errors with different missing data types and tilt/terrain uncertainties

3σ-Position Error (m)								
3σ-tilt (arcsec)	Missing Data		3σ-read (arcsec)		Missing Data		3σ-read (arcsec)	
			60	120			60	120
60	Non-Contiguous	25%	0.34	0.37	Contiguous	25%	0.68	0.76
120			1.63	1.67			2.08	2.16
60		50%	0.37	0.37		50%	1.66	1.87
120			1.68	1.69			4.13	4.49
60		75%	0.37	0.50		75%	12.10	16.15
120			1.72	1.68			20.67	21.84

One of the significant questions regarding the STO technique is its ability to perform accurate prediction when the user is on a flat surface. To address this issue, we investigate whether errors are terrain-dependent, especially since rovers prefer to drive in areas where nearby terrain is primarily benign. Namely, we want to tie the position errors to the user's locations. Figure 10 shows the magnitude of the error at different locations. There are 10,000 locations randomly distributed in the region of interest. The errors are color-coded. The gray dots indicate there are no errors in predicting the pixels. The color codes vary from dark blue (0-10m) to dark red (90-100m). It can be seen from Figures 7 and 10 that when missing data is non-contiguous (STO profile-preserved), the errors are more likely to happen in areas where land is relatively flat. However, the errors do not exceed 20m with a 3σ value less than 2m and predominantly zero errors. The errors for the case where ¾ of the field of view is obstructed, on the other hand, are independent of the flatness of the terrain with the absolute maximum of 90m and 3σ value less than 25m. Flat terrain seems to impact the STO only locally, whereas STO is a more far-field phenomenon constructed by gazing off the horizon. In our STO construction, we assume the terrain extends 120km in each azimuthal direction. The STO technique would not work if the Moon were a spheroid. Finding a plateau extending a hundred kilometers without any ridges or craters for the Moon or Mars could be challenging.

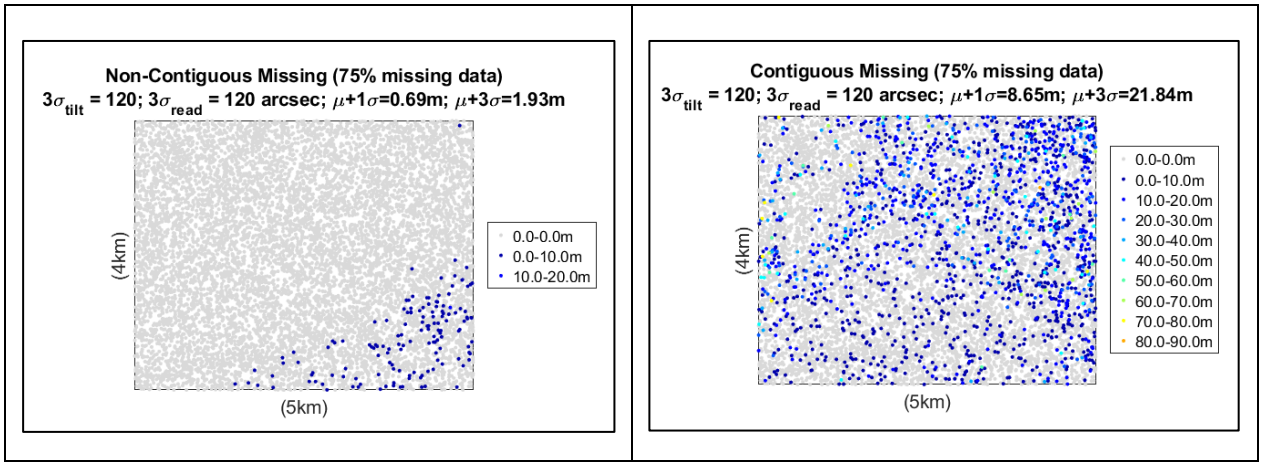

Figure 10: Terrain-dependent errors with 75% non-contiguous (left) and 75% contiguous (right) missing data

6. Summary & Future Work

This paper proposes a hybrid surrounding terrain outline (STO) scheme for real-time autonomous localization without GPS-like infrastructure. With proper optical/infrared sensors, this technique can be implemented day or night. Like other terrain-relative navigation techniques, STO could be time-consuming and require large computer memory and storage, especially when the terrain of interest is large and its spatial resolution is high. This paper proposed a hybrid scheme by first reducing the search space and then applying the STO technique to determine the user's position. A Monte-Carlo simulation was performed using LOLA DEM 5-m terrain data, 120 arcsec tilting and reading errors, and different percentages of missing data. Our results show that even at the worst tilting and terrain uncertainties and half of the field of view being blocked, the 3σ positioning error for the STO is less than 5m. When 75% of the field of view is obstructed, the 3σ positioning errors never exceed 25m. Most importantly, the STO method works in areas with relatively flat local terrain.

Acknowledgements

The research was carried out at the Jet Propulsion Laboratory, California Institute of Technology, under a contract with the National Aeronautics and Space Administration.

References

[1] I. Haase, P. Gläser, J. Oberst, and M. S. Robinson, "Accurate Geolocation of Apollo 17 ALSEP Instruments," European Planetary Science Congress 2012, held 23-28 September 2012 in Madrid, Spain. http://meetings.copernicus.org/epsc2012, id. EPSC2012-74

[2] Cozman, F., Krotkov, E. (1997). Automatic mountain detection and pose estimation for teleoperation of lunar rovers. In: Casals, A., de Almeida, A.T. (eds) Experimental Robotics V. Lecture Notes in Control and Information Sciences, vol 232. Springer, Berlin, Heidelberg. https://doi.org/10.1007/BFb0112963

[3] Cozman, F., Krotkov, E. & Guestrin, C. Outdoor Visual Position Estimation for Planetary Rovers. Autonomous Robots 9, 135–150 (2000). https://doi.org/10.1023/A:1008966317408

[4] C. F. Olson and L. H. Matthies, "Maximum likelihood rover localization by matching range maps," Proceedings. 1998 IEEE International Conference on Robotics and Automation (Cat. No.98CH36146), Leuven, Belgium, 1998, pp. 272-277 vol.1, doi: 10.1109/ROBOT.1998.676398.

[5] Li, R., et al. (2006), Spirit rover localization and topographic mapping at the landing site of Gusev crater, Mars, J. Geophys. Res., 111, E02S06, doi:10.1029/2005JE002483.

[6] Li, R., et al. (2007), Opportunity rover localization and topographic mapping at the landing site of Meridiani Planum, Mars, J. Geophys. Res., 112, E02S90, doi:10.1029/2006JE002776.

[7] A. V. Nefian et al., "Automatic rover localization in orbital maps," Lunar and Planetary Science XLVIII (2017)

[8] L. Matthies et al., "Lunar Rover Localization Using Craters as Landmarks," 2022 IEEE Aerospace Conference (AERO), Big Sky, MT, USA, 2022, pp. 1-17. Doi: 10.1109/AERO53065.2022.9843714.

[9] A. Cauligi et al., "ShadowNav: Crater-Based Localization for Nighttime and Permanently Shadowed Region Lunar Navigation," 2023 IEEE Aerospace Conference, Big Sky, MT, USA, 2023, pp. 1-12. Doi: 10.1109/AERO55745.2023.10115745.

[10] C. Lee and K. -M. Cheung, "A Novel Autonomous Lunar Self-Localization Technique Based on Local Surrounding Horizon Mask," 2024 IEEE Aerospace Conference, Big Sky, MT, USA.

[11] https://sodern.com/wp-content/uploads/2021/11/Hydra.pdf

[12] M. Abdoli, C. Lee, C. Calavitta, L. Helt, A. Jubb, E. Luz, R. Padgett, X. Wang, “Autonomous Localization Based on Surrounding Terrain Outlines Using Machine Learning Techniques,” Accepted for presentation and publication in the SPACEOPS 2025, the 18th International Conference on Space Operations, May 2025, Montreal, Canada.